



Kent Academic Repository

Cao, Lixia (2024), Hossain, MD Moinul, Li, Jian (2024) and Xu, Chuanlong (2024) *Three-dimensional particle image velocimetry measurement through three-dimensional U-Net neural network*. *Physics of Fluids*, 36 (4). ISSN 1070-6631.

Downloaded from

<https://kar.kent.ac.uk/105746/> The University of Kent's Academic Repository KAR

The version of record is available from

<https://doi.org/10.1063/5.0205872>

This document version

Author's Accepted Manuscript

DOI for this version

Licence for this version

UNSPECIFIED

Additional information

Versions of research works

Versions of Record

If this version is the version of record, it is the same as the published version available on the publisher's web site. Cite as the published version.

Author Accepted Manuscripts

If this document is identified as the Author Accepted Manuscript it is the version after peer review but before type setting, copy editing or publisher branding. Cite as Surname, Initial. (Year) 'Title of article'. To be published in **Title of Journal**, Volume and issue numbers [peer-reviewed accepted version]. Available at: DOI or URL (Accessed: date).

Enquiries

If you have questions about this document contact ResearchSupport@kent.ac.uk. Please include the URL of the record in KAR. If you believe that your, or a third party's rights have been compromised through this document please see our [Take Down policy](https://www.kent.ac.uk/guides/kar-the-kent-academic-repository#policies) (available from <https://www.kent.ac.uk/guides/kar-the-kent-academic-repository#policies>).

This is the author's peer reviewed, accepted manuscript. However, the online version of record will be different from this version once it has been copyedited and typeset.

PLEASE CITE THIS ARTICLE AS DOI: 10.1063/1.5205872

Three-dimensional particle image velocimetry measurement through three-dimensional U-Net neural network

Lixia Cao¹ (曹丽霞), Md. Moinul Hossain³, Jian Li² (李健), Chuanlong Xu^{2*} (许传龙)

¹College of Metrology Measurement and Instrument, China Jiliang University, Hangzhou 310018, China

²National Engineering Research Center of Turbo-Generator Vibration, School of Energy and Environment, Southeast University, Nanjing 210096, China

³School of Engineering, University of Kent, Canterbury, Kent, CT2 7NT, UK

*Corresponding author: chuanlongxu@seu.edu.cn

Abstract: This paper proposes a light field (LF) three-dimensional (3D) particle image velocimetry (PIV) method based on a digital refocused algorithm and 3D U-Net neural network for 3D three-component (3D-3C) velocity measurement. A digital refocused algorithm is used to generate a stack of LF-refocused images of tracer particles for establishing the 3D U-Net. The 3D U-Net is then used for the 3D particle field reconstruction. Based on a pair of 3D particle fields, the 3D-3C velocity field is obtained through a 3D cross-correlation algorithm. Numerical simulations and experiments are conducted to analyze the accuracy and efficiency of the proposed method. The simulation results show that the elongation along the depth direction and the efficiency of the 3D particle field reconstruction are improved by the 3D U-Net. The 3D U-Net also provides a better correlation coefficient. The experimental results show that the reconstruction time of the proposed method is ~220 seconds which is 10 times faster than the LF tomographic PIV. This further demonstrates that the proposed method improves the reconstruction efficiency without affecting the accuracy of velocity measurement.

Keywords: Light field, Particle image velocimetry, 3D U-Net, 3D-3C, 3D particle field

1. Introduction

The tomographic particle image velocimetry (Tomo-PIV) based on a single light field camera (LFC) was first proposed in [1]. In the LFC, due to a microlens array (MLA) placed in front of the CCD sensor, the intensity, direction and position of the particle can be captured simultaneously in a single exposure [2]. Therefore, a single LFC is used in Tomo-PIV to capture the tracer particle images instead of using multi-camera systems [3]. A single LFC to be placed conveniently, which greatly reduces the complexity of the Tomo-PIV [4]. Furthermore, the LFC overcomes the issues of the multi-camera systems such as a high degree of coupling and synchronization of multi-camera systems, making the operation and assembly of the system costly and inconvenient [5]. The single LFC-based Tomo-PIV enables the measurement of fluids through a narrow viewport [6].

The recent studies focus on the LF Tomo-PIV mainly for the calculation of the weight matrix, LFC calibration, improvement of tomographic reconstruction techniques for the 3D particle field and optimization of the LFC parameters. The weight matrix is calculated by the forward and backward ray tracing techniques [1, 7-8]. Usually, the calculation of the weight matrix is time-consuming [4, 8]. Thus, summed line-of-sight (SLOS) and multiplied line-of-sight (MLOS) techniques are used to improve the computational efficiency of the weight matrix [9-10]. The calculation of the weight matrix depends on the optical parameters of the LFC without lens distortion. However, the accuracy of the weight matrix is affected by the lens distortion of the LFC. To achieve an accurate weight matrix, an improved volumetric calibration method is used to achieve accurate pixel positions corresponding to the 3D voxel position [11-13]. To achieve an accurate 3D particle field, the effects of the optical parameters of the plenoptic and the focused LFCs on the tomographic reconstruction quality are studied, and the configuration of the LFC is further optimized [5, 14]. A single LFC combined with a mirror is proposed for the 3D particle field reconstruction [15], where the mirror produces two different views that are captured by a single LFC simultaneously. However, it records the flow field in two different views by using a single camera, which sacrifices the spatial resolution of the camera. Therefore, the flow field size captured by the mirror along with the LFC is smaller than that of the single LFC. The dual LFCs are used for the 3D particle field reconstruction and to mitigate the elongation of the reconstructed particle in the depth directions. This provided a better reconstruction quality compared to a single LFC [16-17]. However, the computational cost especially for the weight matrix calculation and the tomographic reconstruction increases.

Besides, the reconstruction of the 3D particle field using a single LFC and tomographic technique is usually time-consuming and storage-intensive [4, 8], which decreases the measurement efficiency of the 3D-3C velocity field. Simultaneous Algebraic Iterative Technique (SART) and a dense ray tracing (DRT)-based Multiplicative Algebraic Reconstruction Technique (MART) (DRT-MART) are used to accelerate the 3D particle field reconstruction process [14, 18]. However, when the

This is the author's peer reviewed, accepted manuscript. However, the online version of record will be different from this version once it has been copyedited and typeset.

PLEASE CITE THIS ARTICLE AS DOI: 10.1063/1.5205872

particle concentration is high, the 3D particle field reconstruction using a single LFC is still time-consuming. This leads to a low temporal resolution of the velocity field. In the past few years, although the LF Tomo-PIV has made significant progress, the reconstruction efficiency of the 3D particle field achieved by the single LFC is not enough. Besides, the single LFC-based 3D particle field reconstruction is usually elongated along the depth directions (along the optical axis of the LFC system) due to its lower depth resolution.

Deep learning (DL) has recently been applied to flow field diagnosis and other applications [19-22]. In PIV, DL is usually used to replace the traditional cross-correlation algorithm to estimate the velocity field of dense particle motion. A four-layer PIV-deep convolutional neural network (PIV-DCNN) is proposed for the flow velocity field prediction [23]. The simulated particle motion and the particle image deformation methods are used to generate the training data such as particle images and their corresponding velocity field. CNN is used to estimate the velocity field of dense particle motion instead of the traditional cross-correlation algorithms [24-25]. The CNN shows similar results with the traditional cross-correlation algorithms [26]. A super-resolution general adaptive network (SRGAN) is proposed for turbulent velocity field reconstruction [27]. In these studies, the DL is used for predicting the velocity field accurately and shows the advantages of high spatial resolution and calculation efficiency. However, most of the DL-based PIV studies are two-dimensional (2D) and use the conventional camera. There is a lack of studies for full 3D particle reconstruction of the flow field based on DL and a single LFC. The 3D U-Net neural network (3D U-Net) only needs smaller training datasets to realize the recognition, cutting and extraction of representative information of the image [28]. It is widely used in different applications such as segmentation of the hippocampus, brain tumours, human organs, salt dome recognition and extraction, etc. [29]. The 3D U-Net fully considers the connectivity of the cut objects in the 3D volume. Thus, it can directly cut the 3D objects in the 3D volume and improve the segmentation accuracy. So, the LFC combined with the 3D U-Net has the potential to improve the computational efficiency for the 3D particle field reconstruction and increase the 3D particle field reconstruction quality.

In this paper, a LF 3D-PIV technique based on the digital refocused algorithm and the 3D U-Net is proposed for reconstructing and measuring the 3D-3C velocity flow field. The refocused algorithm is developed based on backward ray tracing and used to calculate the stack of LF-refocused images due to its advantages of high computational efficiency. The LFC is used to acquire image datasets and the 3D U-Net is used to reconstruct the focused particle from the stack of LF-refocused images. The reconstruction efficiency and quality of the 3D particle field are achieved by the Expectation-Maximization (EM) tomographic reconstruction and the digital refocused algorithm along with 3D U-Net are numerically compared. A LF 3D-PIV setup is built to verify the applicability and feasibility of the digital refocused

This is the author's peer reviewed, accepted manuscript. However, the online version of record will be different from this version once it has been copyedited and typeset.

PLEASE CITE THIS ARTICLE AS DOI: 10.1063/1.50205872

algorithm along with 3D U-Net. Experiments on a laminar and a submerged water jet flow are carried out. Numerical and experimental results are presented and analyzed.

2. Measurement principle

2.1 Principle of LF camera

Fig. 1 shows the structure of the traditional camera and the LFC. For the traditional camera [Fig. 1(a)], the relation between the object plane and the CCD sensor plane meets the conjugate relation, which can be calculated by

$$\frac{1}{l_1} + \frac{1}{l_2} = \frac{1}{f} \quad (1)$$

where l_1 is the distance between the object plane and the main lens, l_2 is the distance between the main lens and the CCD sensor plane, and f is the focal length of the main lens.

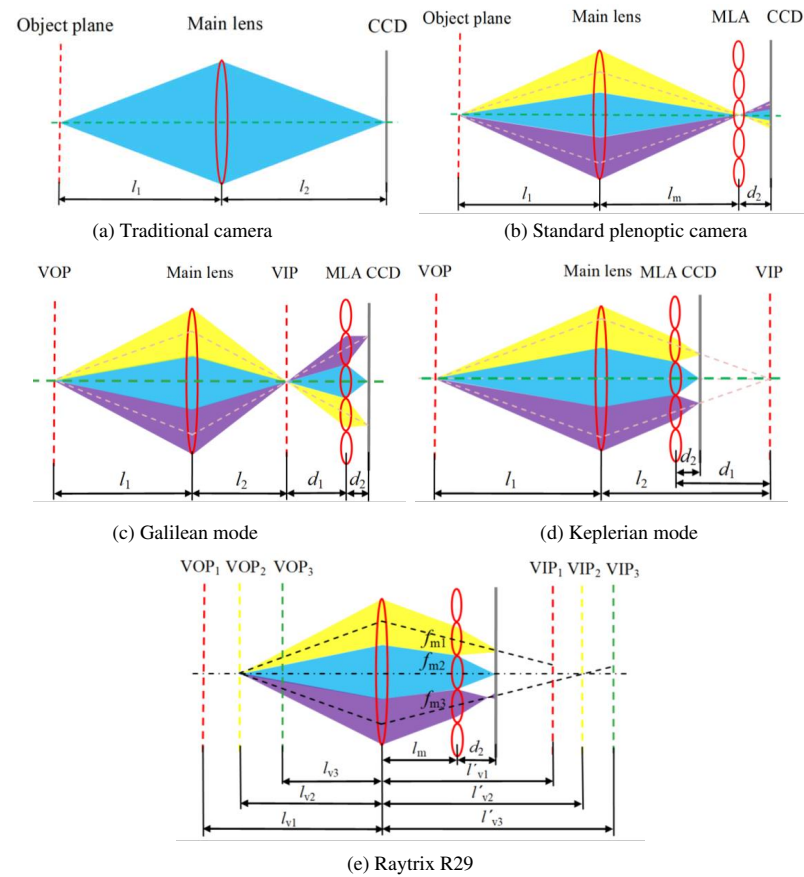


Fig. 1. Structure of the traditional camera and the LFC.

Compared to the traditional camera, the LFC [Fig.1 (b), (c), (d), and (e)] installs a MLA at a specific distance in front of the CCD sensor, allowing the CCD sensor to record the direction and position of the LF at a single snapshot simultaneously. Based on the distance difference between the MLA and the CCD sensor planes, the LFC is generally classified into the standard plenoptic camera (LFC1) and focused LF camera (LFC2) [30]. The LFC1 includes an object plane, main lens, MLA and CCD sensor [31]. The distance between the MLA and the CCD sensor is equal to the focal length of the MLA. The light emitted from a point in object space passes through the main lens and is imaged on a MLA. The MLA images are then transmitted onto the CCD. The main lens is focused on the MLA and the MLA is focused on infinity [32]. Thus, the MLA records the position information of the LF. Simultaneously, the pixel under the MLA (called the sub-image) records the direction information of the LF [33]. The relation between the object plane, main lens, MLA and CCD sensor plane meets the conjugate relation, which can be calculated by

$$\begin{cases} \frac{1}{l_1} + \frac{1}{l_m} = \frac{1}{f} \\ \frac{1}{l_m} + \frac{1}{d_2} = \frac{1}{f_m} \end{cases} \quad (2)$$

where l_m is the distance between the main lens and the MLA plane, f_m is the focal length of the MLA, and d_2 is the distance between the MLA and the CCD sensor.

The structure of the LFC2 includes a virtual object plane (VOP), main lens, MLA, CCD sensor and a virtual image plane (VIP). The LFC2 is generally divided into the Keplerian and Galilean modes based on the positional difference of the VIP [34]. For the Keplerian mode, the distance between the MLA and the CCD sensor is greater than the focal length of the MLA, and the VIP is in front of the MLA. The main lens maps the 3D object outside of the camera into the VIP. Then, the virtual image is remapped into the CCD sensor by the MLA. The MLA records the direction of the LF and the pixel under the MLA records the position of the LF [35]. The relation between VOP, VIP, main lens, MLA and CCD sensor plane meets the conjugate relation, which can be calculated by

$$\begin{cases} \frac{1}{l_1} + \frac{1}{l_2} = \frac{1}{f} \\ \frac{1}{d_1} + \frac{1}{d_2} = \frac{1}{f_m} \end{cases} \quad (3)$$

where l_2 is the distance between the main lens and the VIP, and d_1 is the distance between the VIP and the MLA plane.

For the Galilean mode, the distance between the MLA and the CCD sensor is smaller than the focal length of the MLA, and the VIP is behind the CCD sensor. The relation between VOP, VIP, main lens, MLA and CCD sensor plane meets the conjugate relation, which can be calculated by

$$\begin{cases} \frac{1}{l_1} + \frac{1}{l_2} = \frac{1}{f} \\ \frac{1}{d_2} - \frac{1}{d_1} = \frac{1}{f_m} \end{cases} \quad (4)$$

The LFC1 has a higher depth resolution (along the Z -axis) than the LFC2. LFC2 has a higher lateral resolution (along the X -axis and Y -axis) than the LFC1. Due to the special structure of the LFC, a single LFC replaces the multi-camera system to measure 2D velocity and the 3D velocity fields of the flow.

Compared to the Galilean mode [Fig. 1(e)], the Raytrix R29 LFC has three MLAs with different focal lengths (f_{m1} , f_{m2} and f_{m3}). The relation between VIP, VOP, main lens, MLA and CCD sensor plane meets the conjugate relation, which can be calculated by

$$\begin{cases} \frac{1}{l_{v1}} + \frac{1}{l'_{v1}} = \frac{1}{f} \\ \frac{1}{l_{v2}} + \frac{1}{l'_{v2}} = \frac{1}{f} \\ \frac{1}{l_{v3}} + \frac{1}{l'_{v3}} = \frac{1}{f} \\ \frac{1}{d_2} - \frac{1}{l'_{v2}} = \frac{1}{f_{m2}} \end{cases} \quad (5)$$

where l_{v1} , l_{v2} , and l_{v3} are the distances between the main lens and the VOP1, VOP2 and VOP3, respectively, l'_{v1} , l'_{v2} , and l'_{v3} are the distances between the main lens and the VIP1, VIP2 and VIP3, respectively.

2.2 Proposed method

The proposed method is developed based on LF 3D-PIV, a digital refocused algorithm along with a 3D U-Net neural network for the 3D-3C velocity flow field measurement as shown in Fig. 2. Small tracer particles are first immersed in the measurement volume. A pulse volumetric laser light source is used to illuminate the tracer particles [8, 36]. A pair of LF images of the tracer particles are captured by a single LFC at a time interval. The measurement volume of flow is discretized as a 3D array of the cubic voxel elements in the X , Y , and Z directions, respectively. The refocused algorithm is developed based on a backward ray tracing technique to trace the pixel's line-of-sight (LOS) from the pixel's center to the voxel [8]. Take the Keplerian mode as an example, the backward ray tracing technique includes three steps, such as

Step 1: The coordinate of the intersection point between the pixel's LOS and the main lens can be calculated by

$$y_i = m_y - (l_2 - d_1) \frac{s_y - m_y}{d_2} \quad (6)$$

where m_y is the central coordinate of the MLA along the Y -axis, and s_y is the central coordinate of the sub-image along the Y -axis.

Step 2: The coordinate of the intersection points between the pixel's LOS and the arbitrary voxel plane (marked as the red line in Fig. 2) can be expressed by

$$y_3 = \frac{-l_1 \left[\frac{s_y d_1 - m_y d_1 + d_2 m_y}{d_2} - \frac{z_3 (y_2 - y_1)}{l_1} \right]}{l_2} \quad (7)$$

where z_3 is the distance between the arbitrary voxel plane and the VOP in the Z -axis.

Step 3: When the pixel's LOS intersects the j^{th} voxel, the $3 \times 3 \times 3$ adjacent voxels' intensity distribution of the j^{th} voxel can be calculated by the Gaussian function and expressed by

$$W_{i,j} = A e^{-\frac{d_{i,j}^2}{2\sigma^2}} \quad (8)$$

where σ is the standard deviation and is used to characterise the width of Gaussian distribution, and $d_{i,j}$ is the perpendicular distance between the center of the voxel and the pixel's LOS.

The LF image of tracer particles is then re-projected onto each voxel in the measurement volume and creates a stack of LF-refocused images of tracer particles. The stack of LF-refocused images of tracer particles is elongated and the stack of LF-refocused images includes the focused particle and blurred particle from another voxel plane. The 3D U-Net is trained by the stack of LF-refocused images and then used to reconstruct the 3D particle field. From a pair of reconstructed 3D particle fields, the 3D-3C velocity field is calculated by a 3D cross-correlation technique.

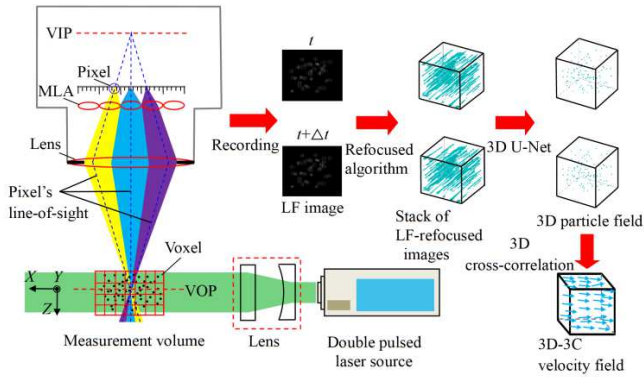


Fig. 2. Strategy of the LF 3D-PIV based on the digital refocused algorithm along with 3D U-Net.

2.3 3D U-Net establishment

The structure of the 3D U-Net model is shown in Fig. 3 [28]. The left side of the 3D U-Net is the analysis path (surrounded by the red dashed lines in Fig. 3) which includes four groups of 3D convolution operations and three down-sampling processes. Each layer uses two $3 \times 3 \times 3$ 3D convolution layers (3D Conv) to extract the feature of the 3D volume, and each convolution is followed by a rectified linear unit (Relu) for correction. A $2 \times 2 \times 2$ 3D max pooling (3D Maxpool) is then used to reduce the size of the 3D feature map. The analysis path can provide essential high-resolution features of 3D volume input to the synthesis path (surrounded by the green dashed lines in Fig. 3). The right side of the 3D U-Net is the synthesis part which is used to reconstruct the 3D volume from the feature map. It also includes four groups of convolution operations and three up-sampling processes. Each layer uses a $2 \times 2 \times 2$ 3D up-convolution (3D up-Conv) to enlarge the feature map of the 3D volume, followed by two $3 \times 3 \times 3$ 3D convolution layers and a Relu. In the final step, a $1 \times 1 \times 1$ 3D convolution is used to reduce the number of output channels to the number of labels.

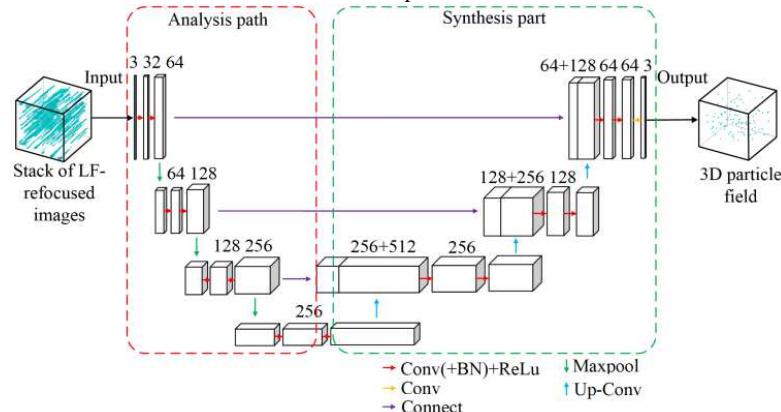


Fig. 3. Structure of the 3D U-Net.

Fig. 4 illustrates a complete process of the 3D particle field reconstruction using the digital refocused algorithm along with the 3D U-Net. The process can be described by

Step 1: 3500 different 3D particle fields are randomly generated at tracer particle concentrations from 0.0031 ppm to 1 ppm. The 3D positional coordinates of tracer particles (X_j, Y_j, Z_j) are then saved.

Step 2: a forward ray tracing technique (linear Gaussian optics) is used to generate the LF image of the 3D particle field based on the coordinates [14].

Step 3: the refocused algorithm is used to obtain the stack of LF-refocused images which are then used as the input data of the 3D U-net.

Step 4: the stack of LF-refocused images includes the focused particle (marked as a red circle in Fig.4) lying at the waist of the stack of LF-refocused images and the blurred particle [37]. The reconstructed particle is characterized by a $3 \times 3 \times 3$ Gaussian-type blob [8]. According to the particle position (X_j, Y_j, Z_j) , the adjacent

$3 \times 3 \times 3$ voxels' intensity distribution of the tracer particle is extracted from the stack of LF-refocused images and is used as the output data of the 3D U-Net.

Step 5: the 3D U-Net is trained and established according to the dataset between the stacks of LF-refocused images and the actual 3D particle fields.

Step 6: the reconstruction of the 3D particle field is performed by the trained model.

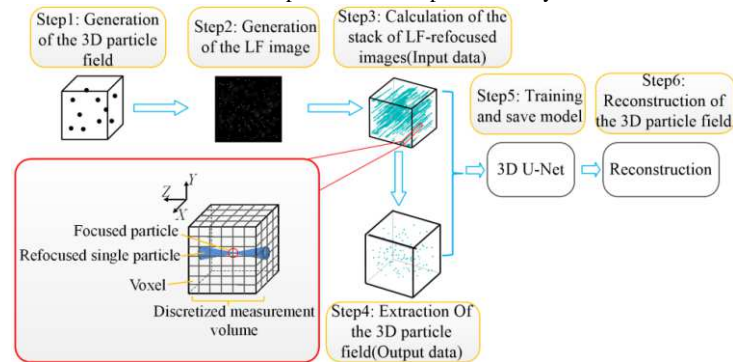


Fig. 4. Reconstruction strategy of the 3D particle field using the proposed method.

3. Numerical simulations

Numerical simulations are performed to validate the reconstruction efficiency and quality of the 3D particle field achieved by the proposed method [i.e., the digital refocused algorithm along with the 3D U-Net]. The proposed method is applied for both the standard plenoptic camera (LFC1) and the Raytrix (R29) for the 3D particle field reconstruction. Thus, the reconstructed 3D particle field between the LFC1 and R29 is compared. The optical parameters of the LFC1 and the R29 used in the simulation are listed in Table 1 [38]. The EM tomographic reconstruction and the proposed method are used for the 3D particle field reconstruction.

Table 1 Parameters of the LFC1 and R29

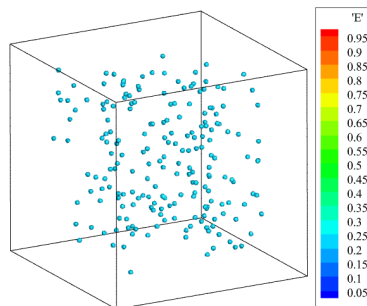
Type of camera	d_2 (mm)	f_m (mm)	f_{m1} (mm)	f_{m2} (mm)	f_{m3} (mm)	f (mm)	l_1 (mm)	l_2 (mm)	l'_2 (mm)	l_m (mm)	P_m (mm)	P_x (μm)
LFC1	0.6	0.6	-	-	-	100	200	-	-	200	0.1705	5.5
						100					0.1705	5.5
R29	1.317	-	1.936	1.626	2.335	100	-	200	200	193.07	0.1705	5.5
						100					0.1705	5.5

In the 3D U-Net, the input and output datasets are the stacks of LF-refocused images and 3D particle fields, respectively. The number of voxels of the 3D particle field is 128 (X -axis) \times 128 (Y -axis) \times 128 (Z -axis). The weights of the 3D U-Net are updated through the Adam optimizer with a learning rate of 0.001 over 30 iterations. The parameters of the Adam optimizer used in this study are $\text{beta}1=0.8$, $\text{beta}2=0.999$, $\text{epsilon}=1 \times 10^{-6}$ and $\text{decay}=0.004$, respectively. A Dice loss function is used to

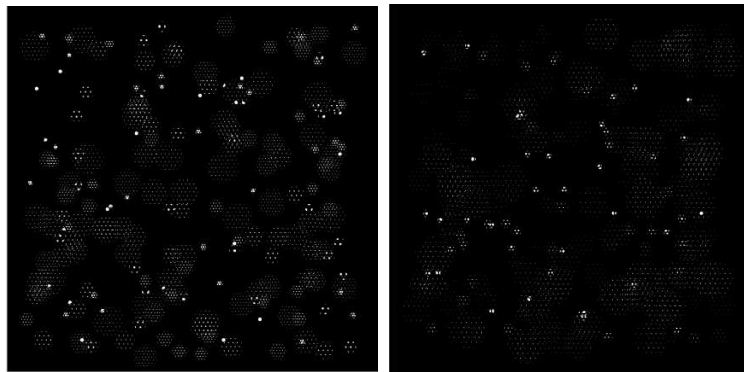
This is the author's peer reviewed, accepted manuscript. However, the online version of record will be different from this version once it has been copyedited and typeset.

PLEASE CITE THIS ARTICLE AS DOI: 10.1063/1.5205872

measure the similarity between two samples. A server with a 36-core Intel (R) Xeon(R) CPU E5-2686 V4@2.3GHz and 128GB RAW is used for the generation of the synthetic LF images of the tracer particles, the calculation of the stack of LF-refocused images of tracer particles, the 3D particle field reconstruction and 3D cross-correlation. A server with an NVIDIA GeForce RTX4090 is used for the 3D U-Net training and testing. The 3D U-Net does not need to calculate a huge weight matrix and the generation of the training datasets is relatively convenient and faster. For the training of the 3D U-Net, 30 iterations are performed and the training time is ~3057 seconds (s) per iteration. Although the 3D U-Net takes ~25.5 hours to establish, once the 3D U-Net is established successfully, it can be used to reconstruct any LF images within a range of particle concentrations.



(a) Reference particle distribution



(b) LFC1

(c) R29

Fig.5. Reference particle distribution and synthetic LF images of the reference particle distribution.

Fig. 5 shows an example of synthetic LF images obtained for the LFC1 [Fig.5(b)] and R29 [Fig. 5(c)] and the reference 3D particle field distributions [Fig. 5a]. The synthetic LF images of the tracer particles of the LFC1 and R29 are generated by the forward ray tracing technique [9, 10]. It can be seen that the different positions of

particles exhibit different particle LF images. The LFC1 has only one type of MLA. Therefore, each MLA has the same defocusing ability for light rays. According to Equation (2), the LF image in the CCD sensor receives the light rays from the main lens plane. The Raytrix R29 LFC has three MLAs with different focal lengths. Therefore, there are three different VIPs, which are the imaging of three different VOPs through the main lens. Different types of MLA produce sub-images with different defocus levels. The EM algorithm and the proposed method are used for the reconstruction of the synthetic LF images, respectively. To reconstruct the 3D particle field by the 3D U-Net model, the stack of LF-refocused images is first calculated by the refocused algorithm. The stack of LF-refocused images is then used as training data for the 3D-Net model.

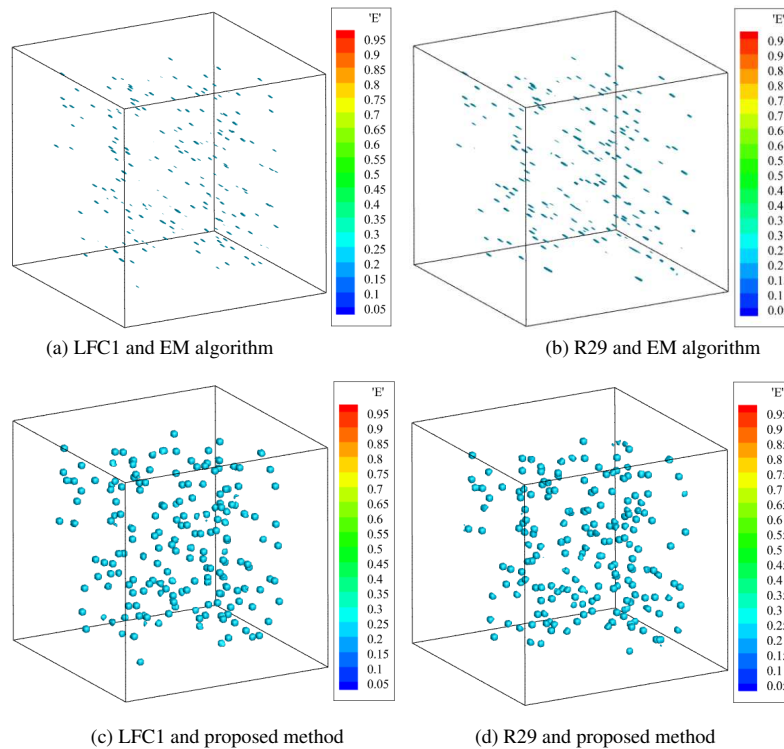


Fig.6. Reconstructed 3D particle field distribution achieved by the proposed method and EM algorithm.

Fig. 6 shows the reconstructed 3D particle field obtained by the EM algorithm and the proposed method. Compared to the reference 3D particle [Fig. 5(a)], the 3D particle fields reconstructed by the EM algorithm are elongated along the depth direction as shown in Fig. 6(a) and (b). The particle elongation is closely dependent on the maximum angle β between pixel's line-of-sights [39]. In the LFC, β is usually less than 20° [5]. Therefore, the reconstructed particle shape is elongated. Particle

distributions achieved by the proposed method are like reference distribution as shown in Fig. 6 (c) and (d). Also, the proposed method shows the alleviation of the elongation of the reconstructed particle along the depth direction compared to the EM algorithm [Fig.6 (a) and (b)].

The overall reconstruction time of the 3D particle field achieved by the proposed method includes the calculation time of the digital refocused algorithm and the prediction time of the 3D U-Net obtained during the reconstruction process. However, the prediction time of the 3D U-Net is almost 0s. Fig. 7 shows the comparison of the overall reconstruction time obtained for the proposed method at different particle concentrations. The calculation time of the digital refocused algorithm is 140s and 150s for the LFC1 and R29, respectively. It can be seen that the calculation time of the digital refocused algorithm is almost constant with the different particle concentrations. Fig. 8 shows the reconstruction time achieved by the EM algorithm. The reconstruction time of the EM algorithm increases with increasing particle concentration. At the particle concentration of 1 ppm, the calculation time of the digital refocused algorithm is within 150s for the LFC1 and R29. However, to complete the whole reconstruction process, the EM algorithm takes ~3200s and 1400s for LFC1 and R29, respectively. Therefore, it demonstrates that the reconstruction efficiency is much higher for the proposed method compared to the EM algorithm.

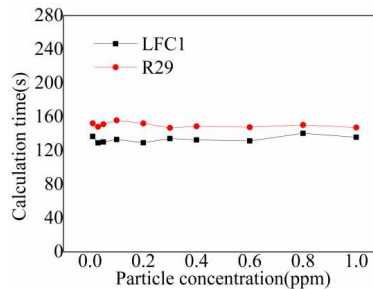


Fig. 7. Calculation time of 3D U-Net.

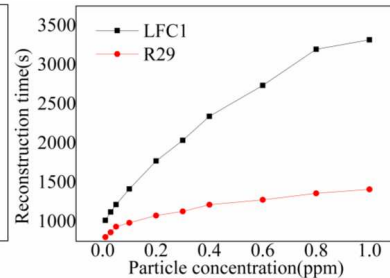


Fig. 8. Comparisons of reconstruction time.

The reconstruction times of the 3D particle field achieved by the EM algorithm and the proposed method under different numbers of voxels at a particle concentration of 0.1 ppm are compared and summarized in Table 2. The reconstruction times achieved by the EM algorithm increase with increasing the number of voxels [8]. When the number of voxels is 301×201×181, the EM algorithm takes tens of thousands of seconds which is very time-consuming. However, the time required for the proposed method is within the 320s. This shows a significant improvement in the reconstruction time.

To evaluate the reconstruction quality of the 3D particle field achieved by the EM algorithm and the proposed method, a normalized correlation coefficient (Q) of the reference and the reconstructed 3D intensity distribution is calculated [40] which is expressed by

$$Q = \frac{\sum_j [E_1(X_j, Y_j, Z_j) \cdot E_0(X_j, Y_j, Z_j)]}{\sqrt{\sum_j E_1^2(X_j, Y_j, Z_j) \cdot \sum_j E_0^2(X_j, Y_j, Z_j)}} \quad (9)$$

where E_0 and E_1 are the reference and reconstructed 3D intensity distribution, respectively. The maximum value of Q is 1, indicating that the reconstructed 3D intensity distribution is equal to the reference 3D intensity distribution.

Table 2 Reconstruction times of 3D particle field when the particle concentration is 0.1 ppm

Number of voxels	EM algorithm (s)	Proposed method (s)
128×128×128	1436	156
301×201×181	10660	305
331×221×151	8072	263

The reconstruction quality of the 3D particle field at different particle concentrations is shown in Fig. 9. The reconstruction quality achieved by the EM algorithm and the proposed method decreases when the particle concentration increases. The Q of the EM for the LFC1 and R29 are less than 0.35 and 0.25 with the particle concentration increases, respectively. The Q of the proposed method is better than the EM algorithm. For the LFC1, when the particle concentration range is 0.01~0.1 ppm, the Q of the proposed method is higher than 0.7. For the R29, when the particle concentration range is 0.01~0.03 ppm, the Q of the proposed method is higher than 0.6. The Q of a single LFC is generally lower than that of multi-camera systems [5, 8]. It shows that the Q achieved by the LFC1 is better than the R29. This is due to the focal length of the MLA of R29 being too long, resulting in low-depth resolution [5].

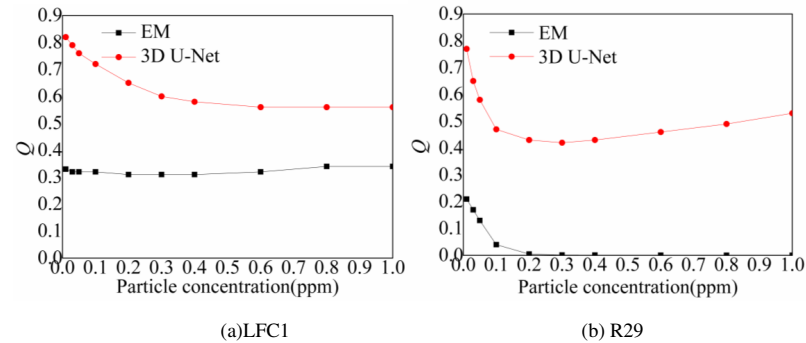


Fig. 9. Comparison of reconstruction quality.

4. Experimental validation

4.1 Measurement of a laminar flow

To verify the applicability and feasibility of the proposed method, experiments were conducted on a laminar flow in a horizontal square pipe. Fig. 10 shows the experimental setup with the associated LF 3D-PIV system components [8]. A laminar

flow is produced by a submersible pump. A stable flow is then controlled by regulating valves 1 and 2. The acrylic channel is a 20mm (Y -axis) \times 18mm (Z -axis) square with a length of 2000 mm (X -axis). The average velocity and the Reynolds number (Re_D) of the laminar are 0.0208 m/s and 389.7, respectively. The flow field is seeded with polyamide particles with a mean diameter of 50 μm , a density of 1.03 g/cm^3 and a particle concentration of 0.5 ppm. The measurement volume is 30mm (X -axis) \times 20mm (Y -axis) \times 18mm (Z -axis) and is illuminated by a double-pulsed laser source with a maximum output energy of 200 mJ per pulse at 532 nm and a pulse duration of 7 ns [8]. The measurement volume is discretized into 301 \times 201 \times 181 voxels. In the 3D cross-correlation algorithm, the 3D cross-correlation window size is set to 48 \times 16 \times 16 with a 50% overlap of interrogation windows.

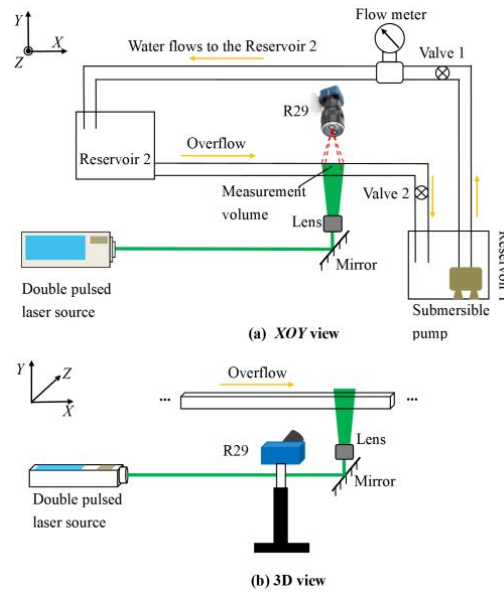


Fig. 10. Schematic of the experimental setup with associated components of LF 3D-PIV system.

The 3D-3C velocity field distribution achieved by the EM algorithm is shown in Fig.11. Fig.12 (a) and (b) show the 1D velocity distributions varying with the Y -axis at the XOY plane and the Z -axis at the XOZ plane corresponding to Fig. 11, respectively. The 3D-3C velocity field distribution achieved by the proposed method is shown in Fig.13. Fig.14 (a) and (b) show the 1D velocity distributions varying with the Y -axis at the XOY plane and the Z -axis at the XOZ plane corresponding to Fig. 13, respectively. The theoretical 1D velocity distributions of the laminar flow varying with the Y -axis at the XOY plane and the Z -axis at the XOZ plane are parabola [8]. From Figs.11, 12, 13 and 14, it can be seen that the 3D-3C velocity field and the parabolic characteristics of laminar flow are successfully measured by the EM algorithm and the proposed method. It shows that all the 1D velocity profiles along the Y -axis are in good agreement with the reference velocity. However, the 1D

This is the author's peer reviewed, accepted manuscript. However, the online version of record will be different from this version once it has been copyedited and typeset.

PLEASE CITE THIS ARTICLE AS DOI: 10.1063/1.5205872

velocity distribution along the Z -axis is poorer than along the Y -axis due to the lower depth resolution of the R29. The maximum velocities of the laminar flow are 0.04 m/s and 0.35 m/s achieved by the EM algorithm and the proposed method near the center of the channel. They correspond to the average velocities of 0.02 m/s and 0.175m/s, respectively. It indicates that the measured laminar velocity is very close to the reference velocity. Note that the theoretical velocity of laminar flow near the edge wall of the pipe is 0 m/s. However, in the actual PIV measurement, the velocity is not 0 m/s and the measured maximum velocity near the center of the channel is less than the theoretical velocity. This is because the cross-correlation calculates the average velocity of a certain window size rather than the velocity of a single point. The measurement results achieved in this study are consistent with Refs. [8, 41].

The reconstruction times of the 3D particle field required by the EM algorithm and the proposed method are also calculated. The time required for the digital refocusing of a LF image is 221s and the 3D U-Net takes 0s to reconstruct the 3D particle field after feeding a stack of LF-refocused images. Thus, the proposed method takes a total reconstruction time of 221 (221+0)s for the 3D particle field. However, the EM algorithm took 73629s, which is very time-consuming. Compared to the EM algorithm, the proposed method significantly improved the reconstruction efficiency of the 3D particle field. Therefore, the laminar flow measurement shows that the efficiency of the 3D particle field is improved significantly by LF 3D-PIV based on the digital refocused algorithm along with 3D U-Net.

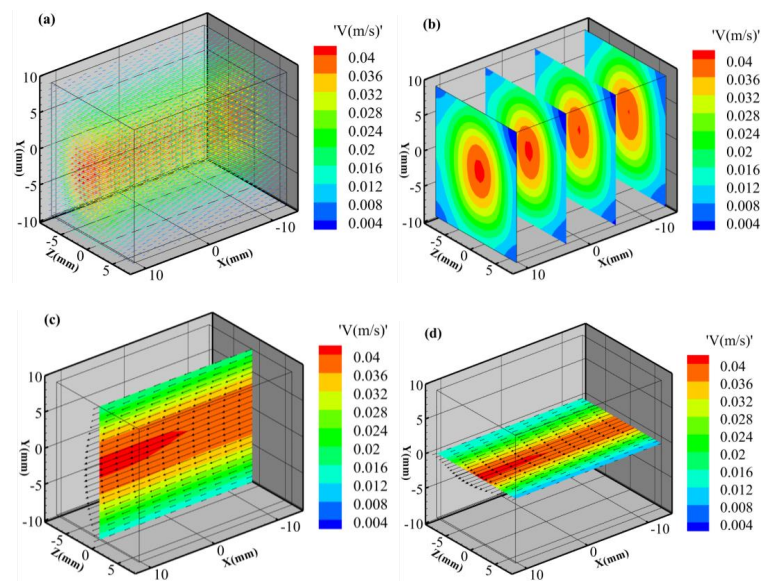


Fig. 11. (a) 3D-3C velocity field by EM algorithm (b) 2D velocity distribution at YOZ plane (c) 2D velocity distribution at XOY plane and (d) 2D velocity distribution at XOZ plane.

This is the author's peer reviewed, accepted manuscript. However, the online version of record will be different from this version once it has been copyedited and typeset.
 PLEASE CITE THIS ARTICLE AS DOI: 10.1063/1.50205872

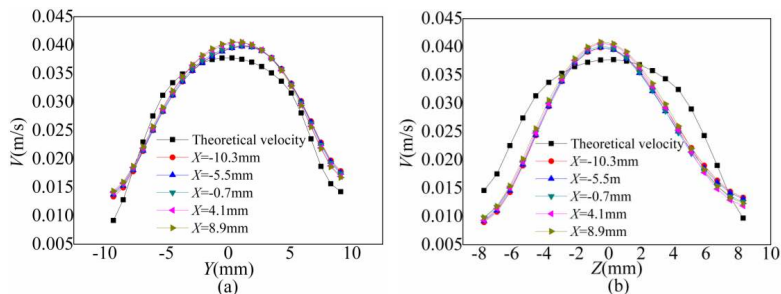


Fig. 12. (a) 1D velocity distributions vary with the Y -axis at the XOY plane and (b) 1D velocity distributions vary with the Z -axis at the XOZ plane.

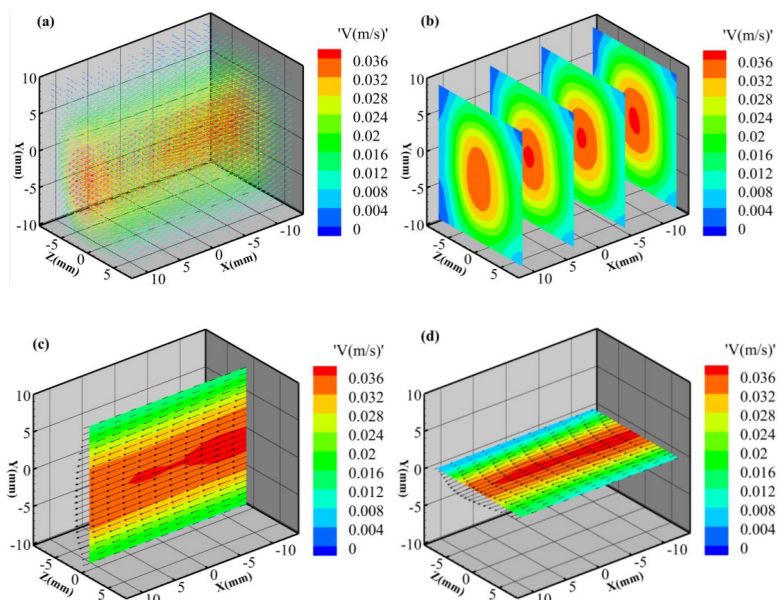


Fig. 13. (a) 3D-3C velocity field by the proposed method (b) 2D velocity distribution at YOZ plane (c) 2D velocity distribution at XOY plane and (d) 2D velocity distribution at XOZ plane.

This is the author's peer reviewed, accepted manuscript. However, the online version of record will be different from this version once it has been copyedited and typeset.

PLEASE CITE THIS ARTICLE AS DOI: 10.1063/1.5205872

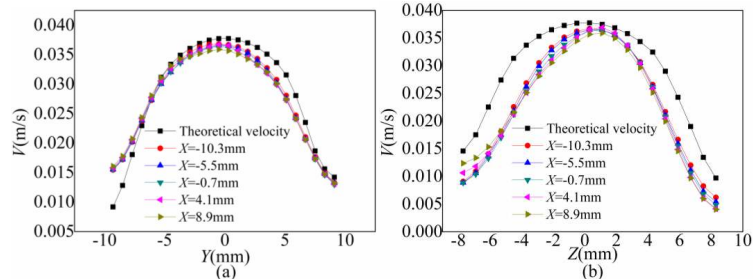


Fig. 14. (a) 1D velocity distributions vary with the Y -axis at the XOY plane and (b) 1D velocity distributions vary with the Z -axis at the XOZ plane.

4.2 Measurement of a submerged water jet flow

The 3D-3C velocity field of a submerged water jet flow is measured by the proposed method. Fig. 15 shows the experimental setup of the submerged water jet flow rig including the assembled LF 3D PIV system and R29. The rig includes a reservoir, valve, flow meter, jet nozzle, submersible pump, double-pulsed laser source and a synchronous controller. The outlet diameter of the jet nozzle is 5.5 mm. The submersible pump pumps purified water from the jet nozzle into the reservoir. The particle concentration is set to 0.5 ppm. The flow rate of the outlet of the jet nozzle is 0.3 L/min in the experiment. The measurement volume is 33.1mm (X -axis) \times 22.1mm (Y -axis) \times 15.1mm (Z -axis) and discretized into 331 \times 221 \times 151 voxels. The voxel size is 0.1 mm. The window size of the 3D cross-correlation is 48 \times 24 \times 24 (X -axis \times Y -axis \times Z -axis). The window size of the overlap is 50%.

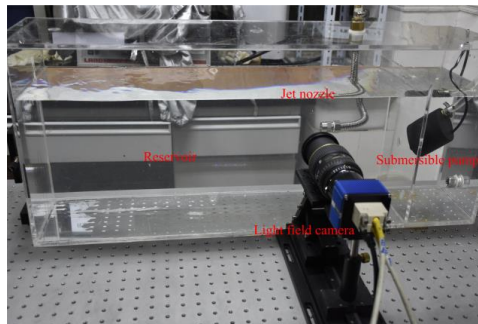


Fig. 15. Experimental setup of the submerged water jet flow rig and assembled LF PIV.

Fig. 16 depicts the 3D-3C velocity field of the submerged water jet flow achieved by the EM. Fig. 16 (b), (c) and (d) show the 2D velocity distribution of the YOZ , XOY , and XOZ planes of the submerged water jet, respectively. Fig. 17 shows the measured 1D velocity field of the submerged water jet corresponding to Fig. 16 (c) and (d), respectively. Fig. 18 shows the 3D-3C velocity field of the submerged water jet flow achieved by the proposed method. Fig. 19 shows the measured 1D velocity

This is the author's peer reviewed, accepted manuscript. However, the online version of record will be different from this version once it has been copyedited and typeset.

PLEASE CITE THIS ARTICLE AS DOI: 10.1063/1.5205872

field of the submerged water jet corresponding to Fig. 18 (c) and (d), respectively. From Figs. 16, 17, 18 and 19, it can be seen that the submerged water jet continues to shoot into the water tank, thereby extending the boundary. From Fig. 16, it can be seen that the initial area of the submerged water jet is located in the area $X=[-15,0]$, $Z=0$ and $Y=0$ mm. The flow rate of the core area of the jet is approximately 4.5 m/s. The submerged water jet is the basic area of the jet in the area of $X=[0,15]$ mm $Z=0$ and $Y=0$ mm, with a flow velocity in the range of 0.5-3.5 m/s, which is lower than that in the initial area. The highest velocity is in the central axis area of the jet. From Fig.17 and Fig. 19, the curve width of the 1D velocity field increases with the increase of the X -axis. It indicates that the width of the outer boundary of the jet increases along the positive X -axis direction, forming a triangular diffusion flow field. The flow velocity of the jet gradually weakens along the positive X -axis direction. The jet flow velocity gradually decreases with increasing $|Y|$ and $|Z|$ ($|Y|$ and $|Z|$ represent the absolute value of Y and Z , respectively). A similar trend is also observed in previous studies [42].

The reconstruction times of the 3D particle field by the EM and the proposed method are calculated. The time required for the refocused algorithm of a LF image is 218s and the time required by the EM algorithm is 48362 s. Compared to the EM algorithm, the proposed method significantly improved the reconstruction efficiency of the 3D particle field.

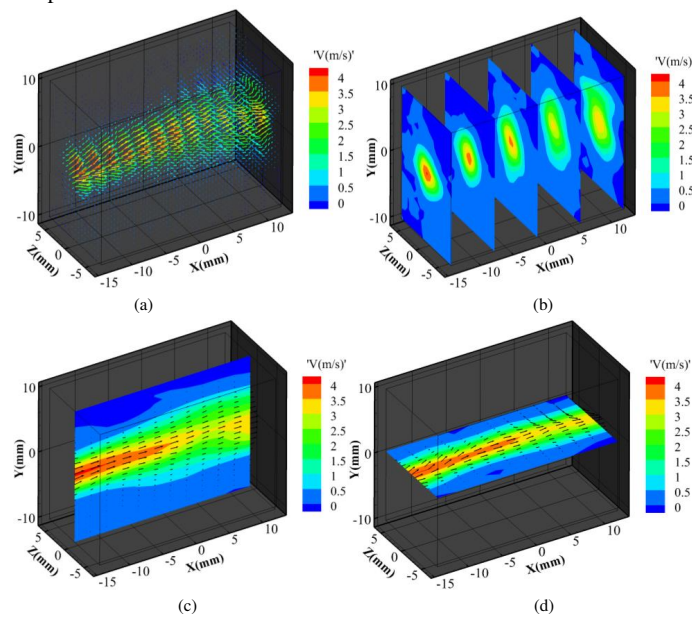


Fig. 16. (a) 3D-3C velocity field by EM algorithm (b) 2D velocity distribution at YOZ plane (c) 2D velocity distribution at XOY plane and (d) 2D velocity distribution at XOZ plane.

This is the author's peer reviewed, accepted manuscript. However, the online version of record will be different from this version once it has been copyedited and typeset.
 PLEASE CITE THIS ARTICLE AS DOI: 10.1063/1.50205872

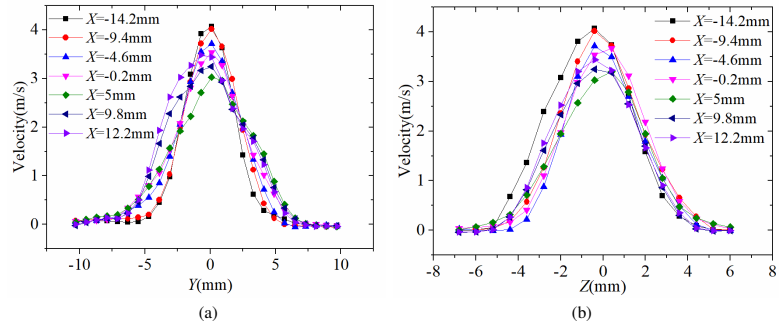


Fig. 17. (a) 1D velocity distributions vary with the Y -axis at the XOY plane and (b) 1D velocity distributions vary with the Z -axis at the XOZ plane.

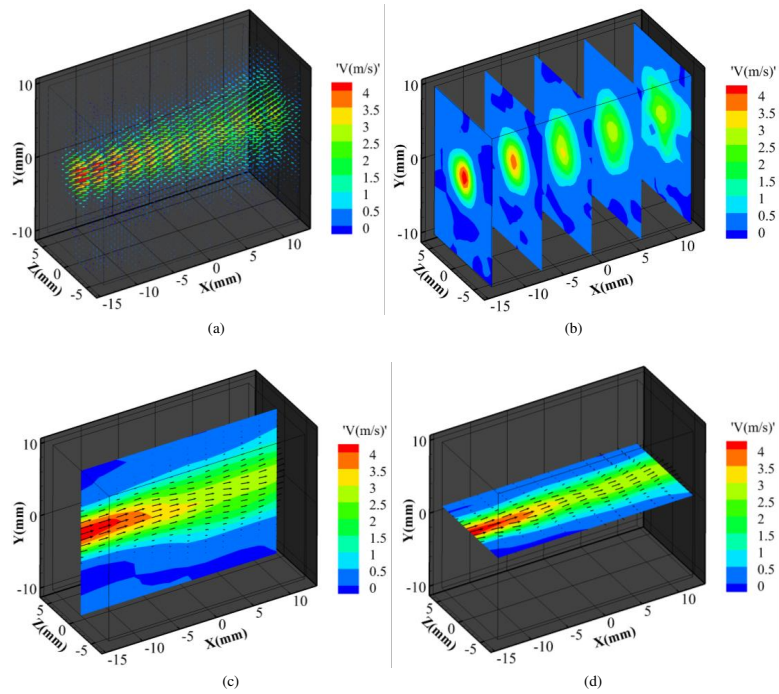


Fig. 18. (a) 3D-3C velocity field by the proposed method (b) 2D velocity distribution at YOZ plane (c) 2D velocity distribution at XOY plane and (d) 2D velocity distribution at XOZ plane.

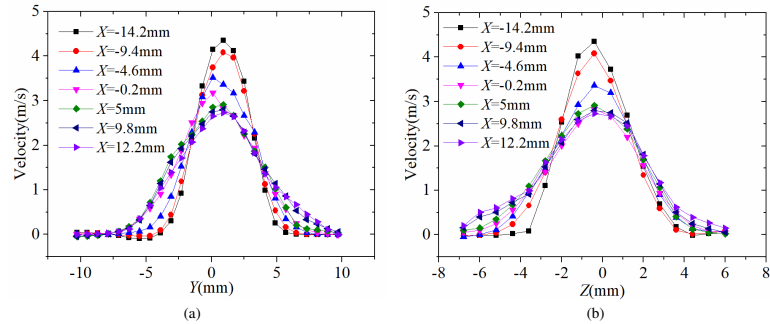


Fig. 19. (a) 1D velocity distributions vary with the Y -axis at the XOY plane and (b) 1D velocity distributions vary with the Z -axis at the XOZ plane.

5. Conclusions

In this paper, a novel LF 3D-PIV based on the digital refocused algorithm along with the 3D U-Net method is proposed to measure the 3D-3C velocity field of the flow field. Numerical simulations were conducted to investigate the reconstruction quality and efficiency of the 3D particle field. Experiments were also conducted to measure the 3D-3C velocity field of a laminar flow and a submerged water jet flow. The main concluding remarks are summarized as follows:

- Simulation results showed that the elongation of the reconstructed particle along the depth and the reconstruction efficiency are improved by the proposed method.
- The reconstruction quality of LFC1 is better than the R29. When the particle concentration is less than 0.1 ppm, the reconstruction quality achieved by the LFC1 is larger than 0.7.
- Experiment results show that the reconstruction time of the proposed method is ~ 220 s without affecting the accuracy of velocity measurement compared with the EM algorithm.
- The proposed method does not require the calculation of the complex weight matrix. The reconstruction time of the proposed method is independent of the particle concentration.

The proposed method provides better results when the LFC1 is used due to its higher depth resolution than the LFC2. In the LF 3D-PIV, the 3D-3C velocity field requires a high-depth resolution (along the Z -axis) for the flow field measurement, thus, the LFC1 is recommended for the flow field measurement. However, if the 3D-3C velocity field requires a high lateral resolution (along the X -axis and Y -axis), the LFC2 is recommended. In the future, the improvement of the depth resolution of LFC and the measurement accuracy of depth direction for LF 3D-PIV will be investigated.

This is the author's peer reviewed, accepted manuscript. However, the online version of record will be different from this version once it has been copyedited and typeset.

PLEASE CITE THIS ARTICLE AS DOI: 10.1063/1.5205872

Acknowledgements. The authors wish to express their gratitude to the National Natural Science Foundation of China (No. 12302370 and 51976038).

CRedit authorship contribution statement

Lixia Cao: Conceptualization, Methodology, Data curation, Writing-original draft.

MD. Moinul Hossain: Technical discussion, Writing-review & editing.

Jian Li: Writing-review & editing.

Chuanlong Xu: Supervision, Project administration, Funding acquisition.

Disclosures. The authors declare no conflicts of interest.

References

- [1] Fahringer T W, Lynch K P, Thurow B S. Volumetric particle image velocimetry with a single plenoptic camera. *Measurement Science and Technology*, 2015; 26(11): 115201.
- [2] Georgiev T, Lumsdaine A. Reducing plenoptic camera artifacts. *Computer Graphics Forum*. Blackwell Publishing Ltd, 2010; 29(6): 1955-1968.
- [3] Lynch K P, Fahringer T W, Thurow B S. Three-dimensional particle image velocimetry using a plenoptic camera. 50th AIAA Aerospace Sciences Meeting Including the New Horizons Forum and Aerospace Exposition, 2012; 1-14.
- [4] Thurow B S, Fahringer T W. Recent development of volumetric PIV with a plenoptic camera. 10th International Symposium on Particle Image Velocimetry, 2013; 1-7.
- [5] Cao L X, Zhang B, Li J, X, Song X L, Tang Z Y, Xu C L. Characteristics of tomographic reconstruction of light-field Tomo-PIV. *Optics Communications*, 2019; 442: 132-147.
- [6] Skupsch C, Brücker C. Multiple-plane particle image velocimetry using a light-field camera. *Optics Express*, 2013; 21(2): 1726-40.
- [7] Shi S X, Ding J F, New T H, Soria J. Light-field camera-based 3D volumetric particle image velocimetry with dense ray tracing reconstruction technique. *Experiments in Fluids*, 2017; 58(7): 78.
- [8] Cao L X, Zhang B, Hossain M M, Li J, Xu C L. Tomographic reconstruction of light field PIV based on backward ray-tracing technique. *Measurement Science and Technology*, 2020; 32(4): 044007.
- [9] Zhu X Y, Hossain M M, Li J, Zhang B, Xu C L. Weight coefficient calculation through equivalent ray tracing method for light field particle image velocimetry. *Measurement*, 2022; 193: 110982.
- [10] Shi S X, Ding J F, New T H. Dense ray tracing based reconstruction algorithm for light field PIV and comparative study with Tomo-PIV. 18th International Symposium on the Application of Laser and Imaging Techniques to Fluid Mechanics, 2016.
- [11] Munz H E, Fahringer T W, Guildenbecher D R, Thurow B S. Volumetric calibration of a plenoptic camera. *Applied Optics*, 2018; 57(4): 914.
- [12] Shi S X, Ding J F, New T H, Liu Y, Zhang H M. Volumetric calibration enhancements for single-camera light-field PIV. *Experiments in Fluids*, 2019; 60(1): 21.
- [13] Zhao Y Y, Li H T, Mei D, Shi S X. Metric calibration of unfocused plenoptic cameras for three-dimensional shape measurement. *Optical Engineering*, 2020; 59(7): 073104.

This is the author's peer reviewed, accepted manuscript. However, the online version of record will be different from this version once it has been copyedited and typeset.

PLEASE CITE THIS ARTICLE AS DOI: 10.1063/1.5205872

- [14] Shi S X, Wang J H, Ding J F, Zhao Z, New T H. Parametric study on light field volumetric particle image velocimetry. *Flow Measurement and Instrumentation*, 2016; 49, 70-88.
- [15] Xing F, He X M, Wang D P, Tan H J. single camera based dual-view light-field particle imaging velocimetry with isotropic resolution. *Optics and Lasers in Engineering*, 2023; 167, 107592.
- [16] Fahringer T W, Thurow B S. Plenoptic particle image velocimetry with multiple plenoptic cameras. *Measurement Science and Technology*, 2018; 29(7): 1-20.
- [17] Mei D, Ding J F, Shi S X, *et al.* High resolution volumetric dual-camera light-field PIV. *Experiments in Fluids*, 2019; 60(8): 132.
- [18] Zhu X Y, Wu Z A, Li J, Zhang B, Xu C L. A pre-recognition SART algorithm for the volumetric reconstruction of the light field PIV. *Optics and Lasers in Engineering*, 2021; 143: 106625.
- [19] Cao C, Liu F, Tan H, *et al.* Deep Learning and Its Applications in Biomedicine. *Genomics, Proteomics & Bioinformatics*, 2018; 16(1): 17-32.
- [20] Teoh K H, Ismail R C, Naziri S, *et al.* Face Recognition and Identification using Deep Learning Approach. *Journal of Physics: Conference Series*, 2021; 1755, 012006.
- [21] Huang J, Liu H, Wang Q, *et al.* Limited-projection volumetric tomography for time-resolved turbulent combustion diagnostics via deep learning. *Aerospace Science and Technology*, 2020; 106123.
- [22] Li Y, Chang J, Kong C, *et al.* Flow field reconstruction and prediction of the supersonic cascade channel based on a symmetry neural network under complex and variable conditions. *AIP Advances*, 2020; 10(6): 065116.
- [23] Li Y, Yang H, Yin Z. PIV-DCNN: cascaded deep convolutional neural networks for particle image velocimetry. *Experiments in Fluids*, 2017; 58(12): 171.
- [24] Cai S Z, Liang J, Gao Q, *et al.* Particle Image Velocimetry Based on a Deep Learning Motion Estimator. *IEEE Transactions on Instrumentation and Measurement*, 2020; 69(6): 3538-3554.
- [25] Cai S Z, Liang J, Zhou S C, Gao Q, *et al.* Deep-PIV: a new framework of PIV using deep learning techniques. *13th International Symposium on Particle Image Velocimetry-ISPIV*, 2019.
- [26] Lagemann C, Lagemann K, Schroder W, *et al.* Deep artificial neural network architectures in PIV applications. *13th International Symposium on Particle Image Velocimetry-ISPIV*, 2019.
- [27] Deng Z W, He C X, Liu Y Z, *et al.* Super-resolution reconstruction of turbulent velocity fields using a generative adversarial network-based artificial intelligence framework. *Physics of Fluids*, 2019; 31: 125111.
- [28] Çiçek Ö, Abdulkadir A, Lienkamp S S, Brox T, Ronneberger O. 3D U-Net: learning dense volumetric segmentation from sparse annotation. *LNCS 9901: Proceedings of the 19th International Conference on Medical Image Computing and Computer-Assisted Intervention*, 2017; 424-432.
- [29] Siddique N, Sidike P, Elkin C, *et al.* U-Net and its variants for medical image segmentation: theory and applications. 2020; 9, 82031-82057.
- [30] Liu Y, Hossain M M, Sun J, Zhang B, Xu C L. Investigation and optimization of sampling characteristics of light field camera for flame temperature measurement. *Chin. Phys. B*, 2019; 3(28): 034207.

This is the author's peer reviewed, accepted manuscript. However, the online version of record will be different from this version once it has been copyedited and typeset.

PLEASE CITE THIS ARTICLE AS DOI: 10.1063/1.5205872

- [31] Zhu X Y, Zhang B, Li J, Xu C L. Volumetric resolution of light field imaging and its effect on the reconstruction of light field PIV. *Optics Communications*, 2020; 462, 125263.
- [32] Georgiev T G. Focused plenoptic camera and rendering. *Journal of Electronic Imaging*, 2010; 19(2): 021106.
- [33] Ng R, Levoy M, Brédif M, *et al.* Light field photography with a hand-held plenoptic camera. *Computer Science Technical Report CSTR*, 2005; 2(11): 1-11.
- [34] Georgiev T G, Lumsdaine A. Depth of field in plenoptic cameras. *Eurographics*, 2009; 5-8.
- [35] Lumsdaine A, Georgiev T G. Full resolution light field rendering. *Indiana University and Adobe Systems, Tech. Rep.*, 2008; 1-12.
- [36] Elsinga G E, Scarano F, Wieneke B, *et al.* Tomographic particle image velocimetry. *Experiments in Fluids*, 2006; 41(6): 933-947.
- [37] Qu X J, Song Y, Jin Y, Guo Z Y, Li Z H, He A Z. 3D particle field reconstruction method based on convolutional neural network for SAPIV. *Optics express*, 2019; 27(8): 11413-11434.
- [38] Chen L, Lei G, Wang T X, Xu C L. Improved blur circle detection method for geometric calibration of multifocus light field cameras. *Optical Engineering*, 2022; 61(9): 093101.
- [39] Scarano F. Tomographic PIV: principles and practice. *Measurement Science & Technology*, 2013; 24(1): 012001.
- [40] De Silva C M, Baidya R, Marusic I. Enhancing Tomo-PIV reconstruction quality by reducing ghost particles. *Measurement Science & Technology*, 2012; 24(2): 1-11.
- [41] Lima R, Wada S, Tsubota K I, Yamaguchi T. Confocal micro-PIV measurements of three-dimensional profiles of cell suspension flow in a square microchannel. *Journal of Biomechanics*, 2006; 39(4): 332-332.
- [42] Staack K, Geisler R. Andreas Schröder. 3D3C-coherent structure measurements in a free turbulent jet. *International Symposium on Application Laser Techniques to Fluid Mechanics. DLR*, 2010.